The Angstrom Project: a microlensing survey of the structure and composition of the bulge of the Andromeda galaxy

E. Kerins,[1]★ M. J. Darnley,[1] J. P. Duke,[1] A. Gould,[2] C. Han,[3] Y.-B. Jeon,[4] A. Newsam[1] and B.-G. Park[4] (The Angstrom Collaboration)

[1]*Astrophysics Research Institute, Liverpool John Moores University, Twelve Quays House, Birkenhead, Merseyside CH41 1LD*
[2]*Department of Astronomy, Ohio State University, 140 West 18th Avenue, Columbus, OH 43210, USA*
[3]*Department of Physics, Institute for Basic Science Researches, Chungbuk National University, Chongju 361-763, Korea*
[4]*Korea Astronomy and Space Science Institute, 61-1, Whaam-Dong, Youseong-Gu, Daejeon 305-348, Korea*

ABSTRACT
The Andromeda Galaxy Stellar Robotic Microlensing Project (The Angstrom Project) aims to use stellar microlensing events to trace the structure and composition of the inner regions of the Andromeda Galaxy (M31). We present microlensing rate and time-scale predictions and spatial distributions for stellar and sub-stellar lens populations in combined disc and barred bulge models of M31. We show that at least half of the stellar microlenses in and around the bulge are expected to have characteristic durations between 1 and 10 d, rising to as much as 80 per cent for brown-dwarf dominated mass functions. These short-duration events are mostly missed by current microlensing surveys that are looking for Macho candidates in the M31 dark matter halo. Our models predict that an intensive monitoring survey programme, such as Angstrom, which will be able to detect events of durations upwards of a day, could detect around 30 events per season within ∼5 arcmin of the M31 centre due to ordinary low-mass stars and remnants. This yield increases to more than 60 events for brown-dwarf dominated mass functions. The overall number of events and their average duration are sensitive diagnostics of the bulge mass, in particular the contribution of low-mass stars and brown dwarfs. The combination of an inclined disc, an offset bar-like bulge, and differences in the bulge and disc luminosity functions results in a four-way asymmetry in the number of events expected in each quadrant defined by the M31 disc axes. The asymmetry is sensitive to the bar prolongation, orientation and mass.

Key words: gravitational lensing – stars: low-mass, brown dwarfs – galaxies: bulges – galaxies: individual: M31 – galaxies: structure.

1 INTRODUCTION

Over the last decade, the microlensing effect has been used to constrain the abundance of compact dark matter in the Milky Way halo (e.g. Alcock et al. 2000; Afonso et al. 2003a). However, some of the most spectacular results have come not from the dark matter surveys but from stellar microlensing surveys directed towards the Galactic bulge, where thousands of events involving ordinary stars have been detected (e.g. Afonso et al. 2003b; Sumi et al. 2003; Popowski et al. 2005; Sumi et al. 2005). The optical depth measured by these surveys has shown that the Milky Way bulge is bar-like and oriented almost towards us, a conclusion supported by near-infrared surveys of the bulge (Dwek et al. 1995). There remains some difference in the reported optical depth of the Milky Way bulge between

red clump giant source sub-samples and full event samples, and this uncertainty partly reflects the difficulty involved in separating foreground disc and bulge lensing populations, blending, and the fact that the number of lines of sight through the bulge is severely restricted due to dust obscuration. Follow-up survey teams, which monitor events alerted in real-time by the main survey teams, have also obtained high signal-to-noise ratio lightcurves for many events, including the spectacular binary event EROS BLG-2000-5, which allowed an accurate mass determination to be made of the lens (An et al. 2002), as well as a detailed limb-darkening profile of the source (Fields et al. 2003). These surveys have also produced the first microlensing detection of a planet (Bond et al. 2004). Microlensing in our own galaxy is now an established tool for planetary, stellar and galactic astrophysics.

With the advent of techniques like difference imaging (Alard & Lupton 1998), it has become possible to look for microlensing events in other galaxies where the sources are unresolved, the
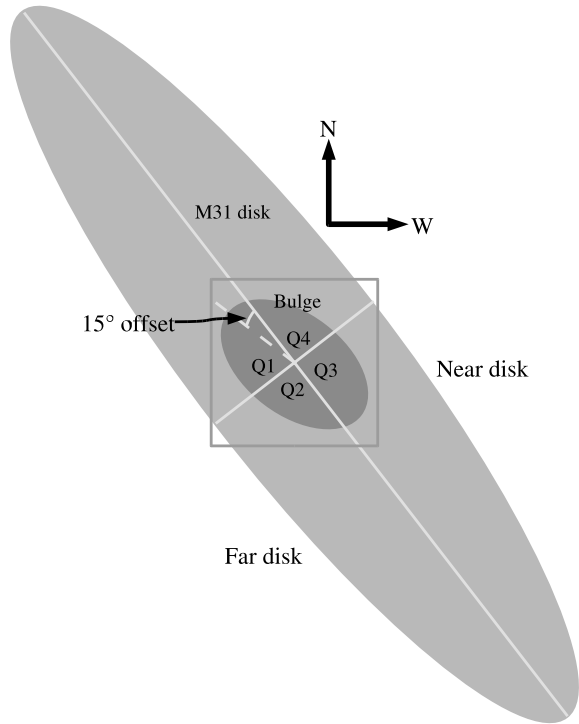
★Email: ejk@astro.livjm.ac.uk

Figure 1. The geometry of the M31 disc and bulge. The disc of M31 is inclined at an angle of 77°, with the north-western side nearer to us. The bulge major axis is taken to be offset on the sky from the disc major axis by 15°, as indicated by the twisting of the inner surface brightness isophotes (Stark & Binney 1994). The M31 disc major and minor axes define four quadrants, labelled Q1–Q4, which are referred to later in this paper. Events involving bulge lenses are expected to occur mainly in quadrants Q1 and Q2 where the disc stars lie behind the bulk of the bulge stars, whilst events involving disc lenses preferentially occur in quadrants Q3 and Q4 where they are in front of the bulk of the bulge stars.

so-called pixel-lensing regime. Several teams (Calchi Novati et al. 2003; Paulin-Henriksson et al. 2003; Riffeser et al. 2003; de Jong et al. 2004; Uglesich et al. 2004; Joshi et al. 2005) are already exploiting this and similar techniques to look for Macho dark matter candidates in the halo of the Andromeda Galaxy (M31). In this paper, we consider how an intensive stellar pixel-lensing survey of the bulge of M31 can be used to probe the stellar mass function and the inner M31 galactic structure. In some respects, we have a better view of the M31 bulge than of our own. The M31 disc is inclined at 77°, so we have a relatively unobscured view of the bulge. M31 is believed to be of earlier type than our own galaxy, and therefore thought to possess a more prominent bulge component. Intriguingly, surface brightness measurements of the central regions of M31 reveal a twisting of the inner optical isophotes (Walterbos & Kennicutt 1987), consistent with a bar-like bulge that is misaligned from the disc major axis by about 15° on the sky (Stark & Binney 1994). The relationship between the M31 disc and bulge is shown schematically in Fig. 1.

The Andromeda Galaxy Stellar Robotic Microlensing Project (Angstrom Project) aims to detect stellar microlensing events in the bulge region of M31. By obtaining upwards of three epochs per 24-h period, the survey will be sensitive to short-duration stellar microlensing events due to low-mass stars and brown dwarfs, which are missed by current M31 microlensing surveys looking for dark matter. Angstrom is using three telescopes in the Northern hemisphere at widely separated longitudes. A pilot season has already

begun with the robotic 2-m Liverpool Telescope on La Palma, the 1.8-m Doyak Telescope at the Bohyunsan Observatory in Korea and the 2.4-m Hiltner at the Michigan-Dartmouth-MIT (MDM) Observatory in Arizona. This paper considers how many events a survey like Angstrom should see, and how their number, time-scales and spatial distribution are sensitive to the low-mass end of the stellar mass function, and to the bulge mass and geometry. Previous studies (e.g. Gould 1994; Han 1996) have considered the optical depth and event rate from simple disc and spheroidal bulge populations. In this study, we make a detailed examination of the pixel-lensing signal expected from a barred bulge based on the survey sensitivity of the Angstrom Project.

The format of this paper is as follows. In Section 2, we discuss the basics of pixel-lensing theory and derive an expression for the pixel-lensing rate for simple analytic distribution functions. In Section 3, we construct a set of five stellar microlensing models comprising a disc and barred bulge. The models reproduce the observed M31 surface brightness and are carefully constructed using consistent assumptions regarding the stellar mass function, luminosity function and resulting mass-to-light ratio. The microlensing predictions from the models are presented in Section 4 and we end with a discussion of the results in Section 5.

2 PIXEL-LENSING THEORY

Pixel lensing differs from classical microlensing in that the sources are unresolved at baseline. Pixel-lensing events are observed as transient local flux enhancements against the background surface brightness. An event is detectable when the lens approaches sufficiently close to the line of sight to an unresolved source. When the lens passes within a fraction u of its Einstein radius, the background source becomes magnified by a factor $A = (u^2 + 2)/[u^2(u^2 + 4)]^{1/2}$, which approximates to u^{-1} for the high-magnification events that comprise the large majority of pixel-lensing lightcurves. Detection is possible when the excess photon count $(A - 1)N_*$ due to the microlensed source star exceeds the local noise, which for bright regions of galaxies is dominated by the galaxy count N_{gal}. For purely Poisson noise, we require

$$(A - 1)N_* \simeq u^{-1}N_* > \alpha N_{\mathrm{gal}}^{1/2}, \tag{1}$$

where $\alpha = 3$ is a typical theorists choice. Equation (1) indicates that for other choices of α the microlensing rate $\Gamma \propto \alpha^{-1}$ because $\alpha \propto u^{-1}$. Let us define u_{t} to be the threshold impact parameter whereby events with a minimum impact parameter $u_0 < u_{\mathrm{t}}$ satisfy equation (1) and so are detectable. These events are detectable for a time-scale

$$t_{\mathrm{v}} = 2\left(u_{\mathrm{t}}^2 - u_0^2\right)^{1/2}\frac{\theta_{\mathrm{E}}}{\mu} = 2\left(u_{\mathrm{t}}^2 - u_0^2\right)^{1/2}t_{\mathrm{E}}, \tag{2}$$

with

$$\theta_{\mathrm{E}} = \left[\frac{4Gm}{c^2 d_{\mathrm{s}}}(l^{-1} - 1)\right]^{1/2} \tag{3}$$

the angular size of the Einstein radius, m the lens mass, d_{s} the distance to the source star and l the distance to the lens in units of d_{s}. Here, G and c denote the standard physical constants. In equation (2), μ is the relative proper motion of the lens across the line of sight and $t_{\mathrm{E}} = \theta_{\mathrm{E}}/\mu$ is the Einstein radius crossing time. We call t_{v} the *visibility time-scale* of the pixel-lensing event. To characterize an event, we must sample with a frequency that is much higher than t_{v}^{-1}. In this study, we examine events with time-scales $t_{\mathrm{v}} > 1$ d, which require a monitoring cadence of several observations per 24-h period. Our choice of a threshold signal of $\alpha = 3$ for this

study represents the significance of the signal at $t_v/2 > 1/2$ d on either side of the peak. The peak of the event is detectable at higher significance than α. Additionally, the signal summed over all data points covering the event has a significance which is much greater than α.

The differential rate of pixel microlensing for lenses of mass m against a given source star can be expressed as

$$d^5\Gamma_m = \frac{u_t}{m} F d_s^5 l^4 \mu^2 \theta_E \, dv_1 \, d\mu \, du \, d\phi \, dl, \qquad (4)$$

where F is the lens distribution function, v_1 is the lens velocity along the line of sight, $u < u_t$ is the lens impact parameter and ϕ describes the random orientation of the lens and source on the sky. Using equation (2) to change variables from μ to t_v, we can re-write equation (4) as

$$d^5\Gamma_m = \frac{8}{m} u_t \left(u_t^2 - u^2\right)^{3/2} F d_s \left(\frac{\theta_E d_s l}{t_v}\right)^4 \, dv_1 \, dt_v \, du \, d\phi \, dl, \qquad (5)$$

from which the event time-scale distribution $d\Gamma_m/dt_v$ can be obtained.

For the models discussed in this paper, we will assume simple distribution functions comprising an analytic density function ρ and an isotropic Maxwellian velocity distribution. That is

$$F = \frac{\rho}{(2\pi)^{3/2}\sigma^3} \exp\left[-\frac{\left(v_t^2 + v_1^2\right)}{2\sigma^2}\right], \qquad (6)$$

where ρ has a functional form yet to be specified, v_t is the velocity across the line of sight and σ is the one-dimensional velocity dispersion. Equation (5) can then be integrated to give the time-scale distribution

$$\frac{d\Gamma_m}{dt_v} = \frac{32\,\sigma}{m} \int_0^1 \int_0^{u_t} \frac{u_t \rho(l)\gamma^4}{\left(u_t^2 - u^2\right)^{1/2}} \exp(-4\gamma^2)$$
$$\times I_0(4\gamma\delta) \exp(-\delta^2) \, dl \, du, \qquad (7)$$

where $I_0(x)$ is the zeroth-order modified Bessel function, $\gamma = \theta_E l d_s (u_t^2 - u_0^2)^{1/2}/\sqrt{2}\sigma t_v$ and $\delta = \mu_{sys} l d_s/\sqrt{2}\sigma$, with μ_{sys} the proper motion of the line of sight. When considering a range of lens masses, we must integrate the time-scale distribution over the lens mass function $\psi(m)$:

$$\frac{d\Gamma}{dt_v} = \frac{\int_{m_l}^{m_u} (d\Gamma_m/dt_v)\, \psi(m)\, dm}{\int_{m_l}^{m_u} \psi(m)\, dm}, \qquad (8)$$

where m_l and m_u are the lower and upper lens mass cut-offs, respectively. The integral of $d\Gamma/dt_v$ over t_v then provides the pixel-lensing event rate per source, Γ.

From equation (1), we can see that u_t depends upon both the source luminosity and the background surface brightness. Moreover, $d\Gamma/dt_v$ is also sensitive to the source distance d_s. Therefore, a full evaluation of $d\Gamma/dt_v$ at a single time-scale t_v and along a single line of sight involves solving a five-dimensional integral over l, d_s, u, m and source luminosity. An evaluation of Γ over the whole bulge region requires two further integrals over t_v and galaxy surface brightness. We evaluate the integrals over l, d_s, t_v and surface brightness via direct numerical integration, whilst the integrals over u, m and source luminosity are performed using Monte Carlo techniques.

A further complication is that equation (1) and subsequent formulae strictly hold only if the source star can be assumed to be point-like, that is to say its angular size $\theta_* \ll u\theta_E$. This approximation may break down when bright giant stars are microlensed by low-mass brown dwarfs in the disc or bulge. In this finite-source regime,

there is differential magnification across the face of the source star and so the overall magnification is evaluated by integrating the microlensing magnification over the source. In our calculations, we explicitly take account of finite source effects when necessary.

Previous pixel-lensing calculations have been based upon the full-width half-maximum time-scale $t_{1/2}$ rather than t_v (e.g. Kerins et al. 2001; Baltz, Gyuk & Crotts 2003), and have been tailored to surveys with a cadence of ~1 observation per 3 d, so they do not apply to the high-cadence survey we are considering here. The main advantage of using t_v rather than $t_{1/2}$ is that it defines what is a detectable event and what is not, and is easily related to the survey cadence; so the efficiency of different sampling strategies can be readily gauged from the predicted time-scale distribution. However, the disadvantage of using t_v is that it depends upon the noise level, which may vary from epoch to epoch, so similar events may have different t_v time-scales at different times. The relationship between t_v and $t_{1/2}$ is also not monotonic and for high magnifications is given by

$$\frac{t_v}{t_{1/2}} = \left(\frac{u_t^2 - u_0^2}{3u_0^2}\right)^{1/2}, \qquad (9)$$

making comparison between the two sets of calculations difficult.

3 SIMPLE MODELS FOR THE M31 INNER GALAXY

Microlensing predictions necessarily depend upon the choice of model one makes for the lens and source populations. There is a good deal of uncertainty in some of the key parameters, which in itself presents one of the prime drivers for the Angstrom Project. Given this uncertainty, it is sufficient for us to adopt relatively simple models for the M31 stellar population that contain the key parameters we are interested in exploring. To this end, we consider a simple two-component model for the stellar populations in M31 comprising an exponential disc and a barred bulge.

At the first sight, stellar pixel-lensing predictions appear to be at the mercy of several theoretical distributions, many of which are ill constrained or unknown for M31. These include (for both the disc and bulge components) the density and velocity distributions, the stellar and remnant mass functions, and the source luminosity functions. However, these distributions are tightly linked with one another and we can exploit this in order to reduce the parameter space. First, we demand that our bulge and disc models are able to satisfactorily reproduce the observed M31 surface brightness profile along both the major and minor axes. Secondly, we demand that our assumed luminosity and mass functions are consistent with one another, that is to say, our assumed luminosity functions fix the shape of the upper end of our mass functions where the bulk of the light is produced. Thirdly, the low-mass end of our mass functions fixes the density normalizations for the disc and bulge and thereby their mass-to-light ratios, since the light is fixed by the observed surface brightness profile.

We proceed by investigating 'heavy' and 'light' disc and bulge models. The heavy models assume stellar mass functions that extend into the brown-dwarf regime and that contain a significant density in such objects. The light models comprise just ordinary hydrogen burning stars with a mass distribution similar to Milky Way stellar populations. All disc and bulge models also comprise a stellar remnant contribution, and the disc models are assumed to comprise a significant amount of gas which neither provides sources nor lenses for microlensing. The mass-to-light ratio implied by the adopted mass functions, along with the gas and remnant contributions, sets the density normalization for each component by the requirement

that the combined light from the disc and bulge satisfactorily reproduces the M31 surface brightness profile along the major and minor axes.

3.1 Density and velocity distributions

Our first component is the disc, for which we adopt a conventional double-exponential profile:

$$\rho_d = \rho_{d,0} \exp(-R/h) \exp(-|z|/H), \tag{10}$$

where $\rho_{d,0}$ is the central disc density, $h = 5.8$ kpc is the disc scale-length, $H = 0.4$ kpc is the scale-height, and R and z are cylindrical coordinates. For our heavy disc, we find $\rho_{d,0} = 0.3\,M_\odot\,\mathrm{pc}^{-3}$ gives an R-band mass-to-light ratio $(M/L_R) = 3$ and reproduces well the M31 surface brightness away from the bulge, whilst for the light disc model we set the normalization a factor of 3.4 times lower.

Disc lenses and sources are assumed to orbit the disc with a circular speed of 235 km s^{-1} beyond 1.25 kpc (5 arcmin) of the M31 centre. Inside 1.25 kpc, the disc is taken to be a solid body rotator. Stars in the heavy disc are assumed to have random motions described by the Maxwellian velocity distribution in equation (6), with a mean one-dimensional dispersion in the transverse direction of $\sigma = 60$ km s^{-1} at $R = 2h$, a position roughly equivalent to the location of the Sun in the Milky Way; for the light disc, we assume a dispersion that is a factor of $\sqrt{3}$ lower than this. For other cylindrical distances R the velocity dispersion is scaled by $\exp[1 - (R/2h)]$, that is by the square root of the mid-plane density.

The second component is the bulge. The twisting of the optical isophotes in the inner regions of M31 clearly indicates that the M31 bulge is barred and with a major axis which is offset by some 15° on the sky from the M31 disc major axis (Stark & Binney 1994), as illustrated schematically in Fig. 1. The surface brightness profile of galactic bulges and elliptical galaxies is typically observed to follow the de Vaucouleur exponential $R^{1/4}$ law (Wyse, Gilmore & Franx 1997). However, in the inner regions a power-law profile with surface brightness $I \propto R^{-\alpha}$ is often observed (Binney & Merrifield 1998), implying a volume density fall-off $\rho \propto R^{-(1+\alpha)}$. We will consider two possible profiles, one an exponential and another a power law. Both distributions are modelled as bars that are offset from the M31 disc major axis.

For the exponential bulge, we adopt the following distribution:

$$\rho_b = \rho_{b,0} \exp\left\{-\left[(x_b/a)^2 + (y_b/qa)^2 + (z_b/qa)^2\right]^s\right\}, \tag{11}$$

where $a = 1$ kpc is the bulge scalelength, $s = 0.75$ is a power-law index, $q = 0.6$ defines the bar prolongation and x_b, y_b and z_b are Cartesian coordinates aligned along the bar principal axes, with z_b normal to the disc plane. The choice of a and s provides a good fit to the surface brightness profile within 10 arcmin, the region in which we are interested, though the fit becomes poorer at larger radii (see top panel of Fig. 2). For the heavy bulge, we fix $\rho_{b,0} = 12\,M_\odot\,\mathrm{pc}^{-3}$ giving $M/L_R = 7$ and a bulge mass of $3.6 \times 10^{10}\,M_\odot$, which is towards the upper end of favoured mass estimates (cf. Kent 1989; Widrow, Perrett & Suyu 2003). For the light bulge, the density is 3.4 times lower, which is at the lower end of the range of mass estimates and is comparable to the inferred mass of the Milky Way bulge (Dwek et al. 1995).

For the power-law distribution, we take

$$\rho_b = \rho_{b,0}\left\{1 + \left[(x_b/a)^2 + (y_b/qa)^2 + (z_b/qa)^2\right]\right\}^{-s/2}. \tag{12}$$

Here, we adopt $a = 0.75$ kpc, $q = 0.6$ and a power-law index $s = 3.5$. The parameters s and a are chosen to allow a good match to the shape of the observed major- and minor-axis surface brightness
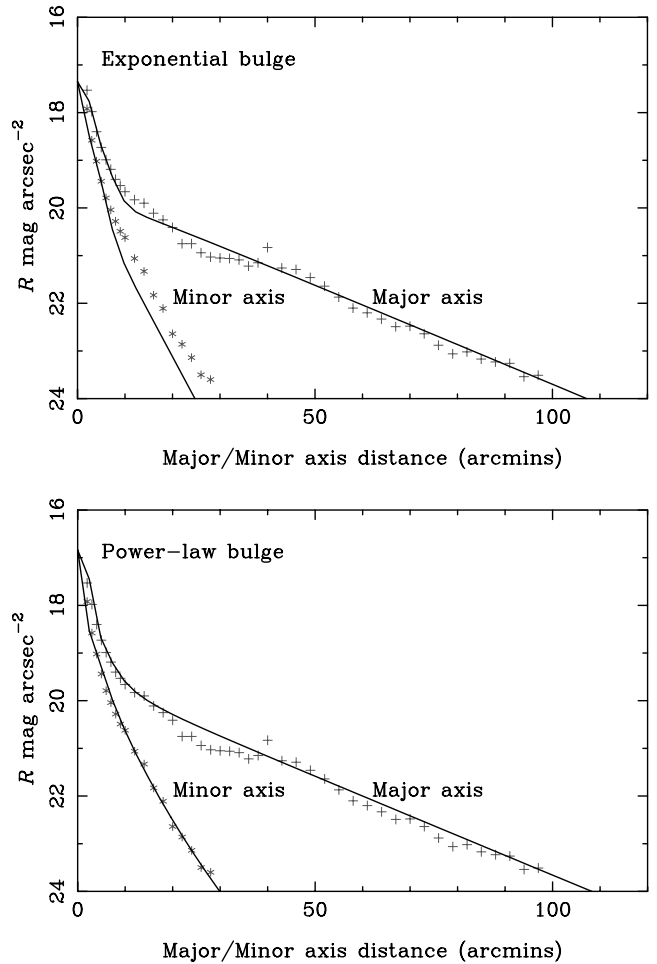

Figure 2. Major- and minor-axis surface brightness profiles predicted for Models 1–4 involving an exponential bulge (top) and for Model 5 involving a power-law bulge (bottom). The model fits are shown by the solid lines whilst the crosses are R-band data for the south-western major axis and south-eastern minor axis from Walterbos & Kennicutt (1987). The exponential bulge model fit is evidently poor beyond 10 arcmin along the minor axis, but is a good fit within the inner bulge region of interest in this paper.

profiles (bottom panel of Fig. 2). The density normalization for the power-law bulge is fixed at $\rho_{b,0} = 6\,M_\odot\,\mathrm{pc}^{-3}$, giving a total mass of $2.1 \times 10^{10}\,M_\odot$, intermediate to the heavy and light exponential bulge, though $M/L_R = 2.1$ which is the same as for the light exponential bulge.

The R-band surface brightness distribution predicted by the combined disc and exponential bulge model is shown in the upper panel of Fig. 2, whilst the lower panel shows the combined disc and power-law bulge profile. Also shown are R-band surface brightness measurements along the major and minor axis of the M31 disc made by Walterbos & Kennicutt (1987). The distributions in equations (11) and (12) differ dramatically at large distances from the bulge centre. The exponential profile gives a considerably poorer fit than does the power-law profile at distances beyond 10 arcmin along the M31 minor axis. However, the two distributions are necessarily similar at smaller distances within the region of interest to us, with the power-law bulge having a slightly brighter peak.

The bulge stars are taken to have Maxwellian random motions according to equation (6) with $\sigma = 90$ km s^{-1} for the light exponential bulge, a factor of $\sqrt{2}$ higher for the power-law bulge

and a factor of $\sqrt{3}$ higher for the heavy exponential bulge. The dispersions are consistent with the range of $\sigma = 100$–150 km s^{-1} observed by McElroy (1983). The bulge velocity dispersion could well differ significantly along each of the principal axes of the bar, so our chosen σ represents the square root of the mean two-dimensional transverse dispersion. We also adopt a bar pattern speed of 57 km s^{-1} kpc^{-1} out to 3.2 kpc (Stark & Binney 1994), capping the circular speed at 180 km s^{-1} outside of this.

We have checked that the mass distribution of our combined bulge and disc models does not exceed that allowed by M31 rotation curve measurements, but we do not attempt to fit our models to the rotation curve as this process inevitably depends on the dark halo profile, which is ill constrained in the inner regions of M31. Instead, the mass normalization of our models is based upon a careful calibration of the stellar mass and luminosity functions which we now discuss.

3.2 Source luminosities

From equation (1), the intrinsic luminosity of the sources is a key factor in detecting pixel-lensing events. Fainter sources are more numerous but require higher magnification in order to be detected. The expected rate of pixel lensing therefore depends on the luminosity function of the sources, but tends to be dominated by the brighter stars.

The luminosity function of the M31 bulge region has been explored in several studies (e.g. Davies, Frogel & Terndrup 1991; Rich & Mighell 1995; Jablonka et al. 1999; Stephens et al. 2003). The high stellar densities cause severe blending problems, which hamper accurate calibrations of the bright end of the stellar luminosity function. In so far as this can be corrected, recent studies find no significant evidence for differences between the bright end of the stellar luminosity function in the M31 and Milky Way bulge regions (Stephens et al. 2003).

We use synthetic colour–magnitude data to model the M31 source stars. These have been generated to match the chemical composition and the mass and luminosity functions observed for stars in the Milky Way disc and bulge, and we assume they provide an adequate description of stars in the M31 disc and bulge. The synthetic data sets are based upon the theoretical stellar isochrones of the Padova group (Girardi & Salaris 2001). The disc and bulge data sets each comprise around a million simulated stars with tabulated masses, ages, bolometric luminosities, effective temperatures and absolute magnitudes in several passbands. The R versus $R - I$ colour–magnitude diagrams for a subset of the disc and bulge stars are shown in Fig. 3.

The main advantage in using synthetic data sets for microlensing calculations is that the radius of each star can be readily computed, and so we can allow for finite source effects in a consistent way. For all but one of our microlensing models, we will assume the M31 bulge sources are described by the synthetic Milky Way bulge stars and the M31 disc sources by the synthetic Milky Way disc stars. For the other model, we assume both bulge and disc sources are described by the synthetic Milky Way disc stars. This allows us to assess the impact of our choice of luminosity function upon the pixel-lensing rate predictions.

We allow for a combined foreground and internal M31 R-band extinction of $A_R = 0.5$ mag when computing the mass-to-light ratio of the source stars. This is equivalent to three times the foreground value (Schlegel, Finkbeiner & Davis 1998) and is consistent with extinction measurements of Sb galaxies using background galaxy counts (Holwerda et al. 2005).
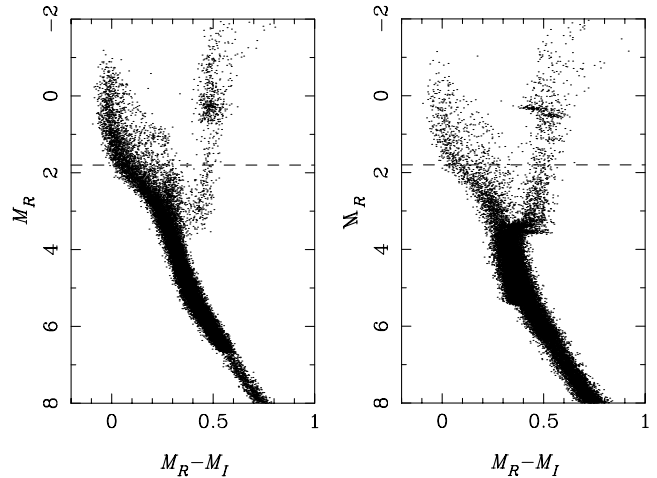

Figure 3. The disc (left-hand side) and bulge (right-hand side) source star synthetic R versus $R - I$ colour–magnitude distributions used for our pixel-lensing calculations. For the Angstrom Project stars above the dashed lines at $M_R = 1.8$ are most likely to act as sources to pixel-lensing events as they require a magnification $A < 30$ to satisfy equation (1) for a background surface brightness $\mu_R = 20$ mag arcsec^{-2}.

3.3 Stellar and remnant mass functions

For our light models, we assume that the bulge and disc mass functions in M31 are similar to those of the Milky Way disc and bulge but do not extend into the brown-dwarf regime. We assume a mass function of the form $\psi(m) = \psi_* + \psi_{\rm rem}$, where ψ_* and $\psi_{\rm rem}$ are the mass functions of the stars and remnants, respectively. The remnant mass function is taken to be a superposition of three Dirac delta functions peaked at 0.6, 1.35 and $5\,M_\odot$, corresponding to white dwarfs, neutron stars and black holes, respectively. The ratio of their mass density contributions is set at $0.7 : 0.2 : 0.1$, respectively. This prescription is a slight simplification of the remnant mass function advocated by Gould (2000).

The stellar mass function ψ_* is modelled by a broken power law:

$$\psi_* = \begin{cases} K(m/m_{\rm t})^{x_1} & (m_{\rm l} < m < m_{\rm t}) \\ K(m/m_{\rm t})^{x_2} & (m_{\rm t} \leqslant m < m_{\rm u}) \end{cases} \tag{13}$$

between lower and upper mass limits $m_{\rm l}$ and $m_{\rm u}$. We set the transition mass at $m_{\rm t} = 0.5\,M_\odot$. The power-law index x_2 and $m_{\rm u}$ is fixed to be consistent with our synthetic stellar population models. Accordingly, we take $m_{\rm u} = 1\,M_\odot$ for bulge stars and $10\,M_\odot$ for disc stars, whilst $x_2 = -2.35$ for both populations. This is the case for both the heavy and light models. For the light bulge and disc, we take $m_{\rm l} = 0.08\,M_\odot$ and $x_1 = -1.4$, which is consistent with observations of the Milky Way bulge mass function (Zoccali et al. 2000). For the heavy models, we instead let $x_1 = x_2 = -2.35$ and extend the mass function down to $m_{\rm l} = 0.03\,M_\odot$ for the bulge and $m_{\rm l} = 0.01\,M_\odot$ for the disc. Different values of $m_{\rm l}$ are needed in order to reproduce the correct M/L_R values for each component, though we could just as easily have used a single value of $m_{\rm l}$ and different values for x_1.

The normalization constant K is fixed by the overall stellar mass density, which contributes a fraction $(1 - f_{\rm rem} - f_{\rm gas})$ of the overall density, where $f_{\rm rem}$ and $f_{\rm gas}$ are the remnant and gas density contributions, respectively. We assume $f_{\rm gas} = 0$ in the bulge and 0.3 in the disc, whilst $f_{\rm rem} = 0.3$ in the bulge and 0.15 in the disc. The values of both $f_{\rm gas}$ and $f_{\rm rem}$ directly affect the computed M/L_R for each population as there is no light contribution from the remnants

Table 1. The M31 disc-bulge models. Parameters for the density and velocity refer to the density distributions in Section 3.1 and the distribution function in equation (6). Parameters for the lens masses refer to the mass functions discussed in Section 3.3. For the disc the quoted velocity dispersion is normalized to its value at cylindrical distance $R = 2h$. Other parameters that are fixed to the same values for all models are discussed in Sections 3.1 and 3.3.

Model	Description	Bulge parameters	Disc parameters	Remarks
1	Light exponential bulge, light disc	$\rho_{b,0} = 3.5\,M_\odot\,pc^{-3}$, $\sigma = 90\,km\,s^{-1}$ $m_1 = 0.08\,M_\odot$, $x_1 = -1.4$ $a = 1\,kpc$, $M/L_R = 2.1$	$\rho_{d,0} = 0.09\,M_\odot\,pc^{-3}$, $\sigma = 35\,km\,s^{-1}$ $m_1 = 0.08\,M_\odot$, $x_1 = -1.4$ $M/L_R = 0.9$	
2	Heavy exponential bulge, heavy disc	$\rho_{b,0} = 12\,M_\odot\,pc^{-3}$, $\sigma = 150\,km\,s^{-1}$ $m_1 = 0.03\,M_\odot$, $x_1 = -2.35$ $a = 1\,kpc$, $M/L_R = 7$	$\rho_{d,0} = 0.3\,M_\odot\,pc^{-3}$, $\sigma = 60\,km\,s^{-1}$ $m_1 = 0.01\,M_\odot$, $x_1 = -2.35$ $M/L_R = 3$	
3	Light exponential bulge, heavy disc	$\rho_{b,0} = 3.5\,M_\odot\,pc^{-3}$, $\sigma = 90\,km\,s^{-1}$ $m_1 = 0.08\,M_\odot$, $x_1 = -1.4$ $a = 1\,kpc$, $M/L_R = 2.1$	$\rho_{d,0} = 0.3\,M_\odot\,pc^{-3}$, $\sigma = 60\,km\,s^{-1}$ $m_1 = 0.01\,M_\odot$, $x_1 = -2.35$ $M/L_R = 3$	
4	Light exponential bulge, heavy disc	$\rho_{b,0} = 4\,M_\odot\,pc^{-3}$, $\sigma = 90\,km\,s^{-1}$ $m_1 = 0.01\,M_\odot$, $x_1 = -2.35$ $a = 1\,kpc$, $M/L_R = 2.4$	$\rho_{d,0} = 0.3\,M_\odot\,pc^{-3}$, $\sigma = 60\,km\,s^{-1}$ $m_1 = 0.01\,M_\odot$, $x_1 = -2.35$ $M/L_R = 3$	Uses disc LF and MF for both bulge and disc
5	Power-law bulge, light disc	$\rho_{b,0} = 6\,M_\odot\,pc^{-3}$, $\sigma = 120\,km\,s^{-1}$ $m_1 = 0.08\,M_\odot$, $x_1 = -1.4$ $a = 0.75\,kpc$, $M/L_R = 2.1$	$\rho_{d,0} = 0.09\,M_\odot\,pc^{-3}$, $\sigma = 35\,km\,s^{-1}$ $m_1 = 0.08\,M_\odot$, $x_1 = -1.4$ $M/L_R = 0.9$	

or the gas. They therefore affect the way in which changes to the stellar mass function translate into changes in the overall density normalization of a given component. Also, the larger the value of f_{rem}, the greater the microlensing contribution from remnant lenses at the expense of stellar lenses, whereas a larger value of f_{gas} reduces the overall microlensing signal since it is at the expense of both the remnant and stellar density contributions.

3.4 The microlensing models

The models we use to compute the pixel-lensing rate are presented in Table 1. Model 1 is the most conservative comprising a light disc and light exponential bulge. Model 2 considers a heavy disc and heavy exponential bulge. Model 3 examines the effect of a light exponential bulge combined with a heavy disc. The purpose of Model 4 is to allow us to explore the effect of the luminosity function on pixel-lensing predictions. It assumes a disc luminosity function and heavy disc mass function for both the bulge and disc populations, though the bulge has the same gas and remnant fraction as for the other bulge models. The resulting mass-to-light ratio is $M/L_R = 2.4$, slightly lower than the heavy disc value. So, whilst the bulge mass function in Model 4 is similar to the heavy bulge model, the bulge mass is closer to that of the light bulge because of the low mass-to-light ratio of the disc-like stellar population. Finally, Model 5 considers a light disc and power-law bulge to allow a comparison between different functional forms for the bulge.

4 MICROLENSING YIELDS

4.1 Model predictions

We base our rate calculations on the parameters of the Angstrom Project, assuming a distance to M31 of 780 kpc (Stanek & Garnavich 1998) and a foreground extinction of $A_R = 0.17$ (Schlegel et al. 1998). The Angstrom Project uses three telescopes, one with an 11-arcmin field of view, the other two with 5-arcmin field of view. The data are being analysed using difference imaging techniques (Alard & Lupton 1998) in which an optimal reference image is constructed from images taken under good seeing conditions and then convolved and subtracted from each target image. The result-

ing difference images record only objects that have varied in their flux. For our calculations, we assume observations are made in the R band and the typical seeing is 1 arcsec. The typical R-band exposure time is set at 600 s, and the detector has a zero point of $R = 24.6$ mag. For a Gaussian source point spread function (PSF), and assuming the noise within the PSF is dominated by the galactic background, the optimal signal-to-noise ratio is obtained by measuring the difference flux out to 71.5 per cent of the encircled energy in the PSF, corresponding to a radius of 0.67 arcsec for our reference image. For guidance, the dashed lines in Fig. 3 indicate the limiting source magnitude assuming the parameters above for the detection of a pixel-lensing event with $A < 30$ and a background surface brightness $\mu_R = 20$ mag arcsec^{-2}.

Fig. 4 shows the spatial distribution of pixel-lensing events with $1\,d < t_v < 100\,d$ for the five models in Table 1. The plots cover a field of view of 11 arcmin centred on the bulge. The cross denotes the centre of M31 and the dotted lines show the orientation on the sky of the major and minor axes of the M31 disc. The contours show the expected number of events per square arcmin per year. For all models, the event distribution is strongly dominated by bulge lenses, as can be seen in Fig. 5, which shows the spatial distribution separately for disc and bulge lenses. The number of events involving disc lenses is typically around three events per season, so it is around order of magnitude lower than the bulge rate even for the heavy disc models. The spatial distributions in Fig. 4 therefore trace the bulge structure and so are noticeably rotated away from the disc axes for all models. Additionally, Models 1–3 clearly show an excess of events towards the far (south-eastern) side of the M31 disc. For these models, a significant fraction of all events involves bulge lenses and disc sources, so we expect their distribution to be skewed towards the far disc. Models 4 and 5 are dominated by events involving bulge lenses and sources, so their distributions appear more symmetric and more closely trace the bar profile.

Fig. 6 shows the time-scale distributions for Models 1–5. The separation between the model predictions is most evident at time-scales $t_v < 10\,d$, emphasising the need for short-time-scale sensitivity. In general, the heavier models produce a higher rate of events and peak at shorter durations. The rate for all models tails off sharply for $t_v > 50\,d$.

Table 2 shows the average duration and the number of events with visibility time-scales between 1 and 100 d expected from a
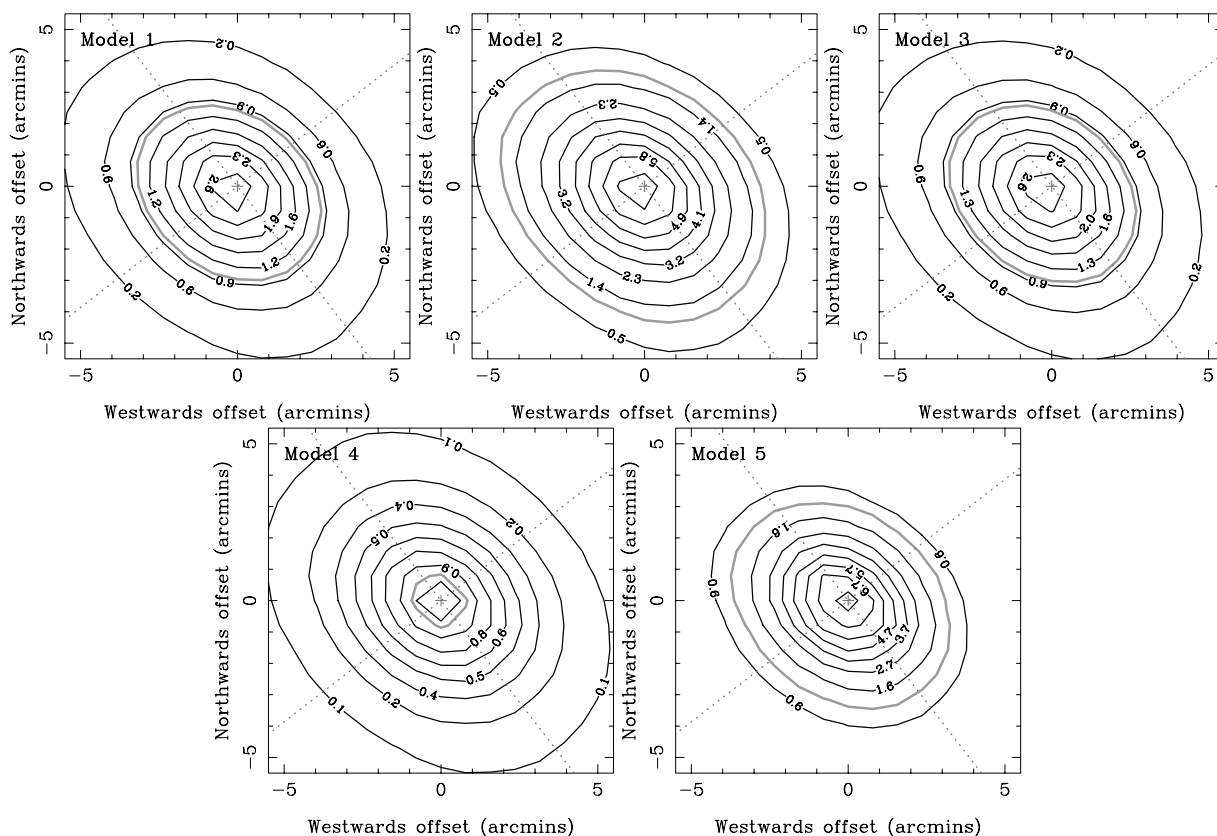
Figure 4. The pixel lensing spatial distribution for Models 1–5 for events with visibility time-scales $t_v = 1$–100 d. The origin of each panel corresponds to the centre of M31 (shown by the cross) and the dotted lines running diagonally demarcate the major (upper left to lower right) and minor (lower left to upper right) axes of the M31 disc. The event rate contours are shown in black and are labelled in events per year per arcmin square. The green contour indicates a level of 1 event per year per arcmin square.

5-month observing season for an 11-arcmin field centred on the M31 bulge. The average duration lies between 7 and 16 d, with heavier bulge models giving rise to shorter events. The shorter durations arise because the mass function for the heavier models extends into the low-mass brown-dwarf regime, and also because the velocity dispersion for the heavier models is larger.

Excluding Model 4, the total number of events with durations between 1 and 100 d ranges from 27 to 64, with the larger yields coming from the heavier, brown-dwarf rich models. The number of short-duration events ($1 < t_v < 10$ d) is also shown in Table 2, ranging from 13 events per season for the lighter models to 50 events per season for the heavy exponential bulge. For the lighter models, about half of all events have durations below 10 d, whilst for the heavier models they comprise up to 80 per cent of all events.

Model 4 assumes a disc luminosity function and heavy disc mass function for the bulge stars. Observations clearly exclude such a luminosity function for the M31 bulge, but the purpose of this hybrid model is simply to assess the effect of changes to the luminosity function on pixel-lensing predictions. It is evident from Fig. 4 and Table 2 that the yield from this model is significantly less than for the others; it is a factor 2 below the conservative Model 1. Naively, this seems a very surprising result given that the bulge sources are brighter for Model 4. Equation (1) indicates that brighter sources can be detected at larger impact parameters, and therefore the rate per source is larger from equation (4). However, the low mass-to-light ratio of the disc-like stars means that we must adopt a

brown-dwarf dominated mass function to give a bulge mass which is compatible with at least the lower end of the preferred M31 bulge mass estimates, whilst satisfying the observed M31 surface brightness. Even with a brown-dwarf dominated mass function, a heavier bulge would be too bright to be consistent with surface brightness observations. The combination of low-mass lenses and bright giant stars typically gives rise to finite source effects which dilute the overall microlensing magnification. For a $0.01\,\mathrm{M}_\odot$ lens lying at a typical distance of 1 kpc in front of the source, a lens–source angular separation of less than $0.04\,\mu$arcsec is required to produce a magnification $A > 10$. At the distance of M31, this corresponds to a separation of just $6\,\mathrm{R}_\odot$, so finite source effects are dominant at these lens masses, resulting in a significant suppression of the microlensing rate for this model. This model is obviously rather extreme, but the basic point is that the boost in the microlensing rate per source due to brighter stars is cancelled out by the lower density normalization required to satisfy surface brightness constraints. So, even if there are no constraints on the permitted mass of the bulge, a boost in the number of bright stars does not result in a gain in the overall microlensing rate.

The number of events expected within each quadrant Q1–Q4 defined in Fig. 1 is also given in Table 2. For Models 1–3, the ratio of the number of events in each quadrant is about $1.6 : 1.5 : 1.2 : 1$ (Q1 : Q2 : Q3 : Q4), whilst for Model 4 it is $1.2 : 1 : 1.2 : 1$ and for Model 5 (the power-law bulge) it is $1.5 : 1.3 : 1.3 : 1$. The number of events in quadrants Q1 and Q2 generally outnumber those in Q3 and Q4 because the M31 disc inclination skews the distribution of
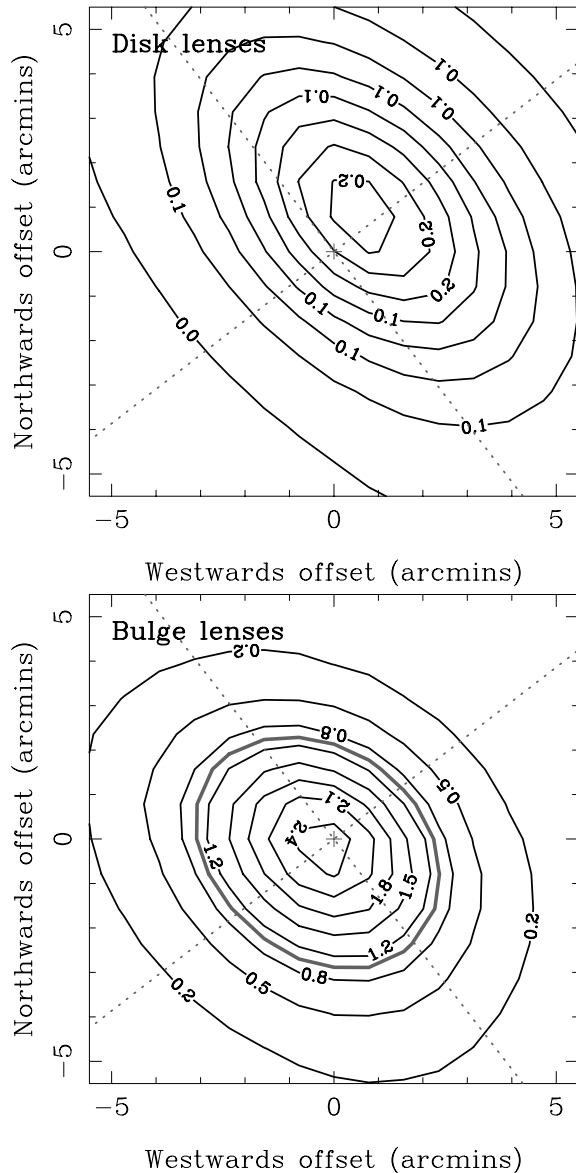
Figure 5. The pixel-lensing spatial distribution in Model 1 for disc (top) and bulge (bottom) lenses. Contours and lines are as for Fig. 4.

bulge lens–disc source events towards the far disc. This along with the offset of the barred bulge away from the disc axis introduces an enhanced asymmetry between events at either end of the bar in Q1 and Q3, giving an overall rise to a four-way asymmetry. The asymmetry is much less evident for Model 4 because the source luminosity and lens mass functions are the same for the disc and bulge, so the rate of bulge lens–disc source events is similar to the rate of disc lens–bulge source events. For the other models, the strength of this four-way asymmetry depends upon the bar offset, the degree of bar prolongation and the mass of the bar, so it is a good signature with which to probe the bar geometry. For the Models 1–3, a sample of around 28 events would be needed in Q4 in order to detect a difference with Q1 at the 95 per cent confidence level. Such a difference should therefore be detectable within three to six seasons, depending on the model. However, a much more efficient strategy is simply to undertake a likelihood analysis of the positions and time-scales of the entire sample in order to constrain the bar parameters.
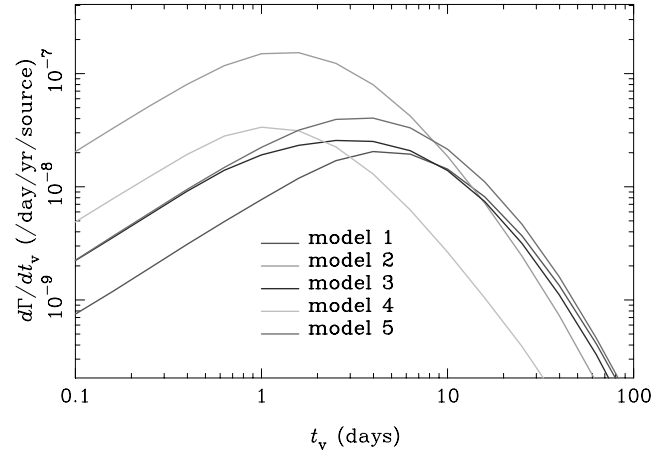

Figure 6. The rate-weighted pixel-lensing time-scale distribution for Models 1–5 for an 11-arcmin field of view centred on the M31 bulge. The models are most distinguishable for time-scales $t_v < 10$ d. Angstrom will be sensitive to events with $t_v > 1$ d.

Table 2. Event yields for the Angstrom Project. $\langle t_v \rangle$ refers to the average visibility time-scale for events in the range $1\,\mathrm{d} < t_v < 100\,\mathrm{d}$. N refers to the number of events per 5-month season over an 11-arcmin field centred on the M31 bulge (as in Fig. 4). Angstrom is also using telescopes with 5-arcmin fields, for which the expected yields are about half of that quoted below. Yields are also presented separately for the eastern (Q1), southern (Q2), western (Q3) and northern (Q4) quadrants defined in Fig. 1.

Model	$\langle t_v \rangle$(d)	N(1–100 d)					N(1–10 d)
		Q1	Q2	Q3	Q4	Total	
1	16	8	8	6	5	27	13
2	7	19	17	16	12	64	51
3	14	8	8	7	5	28	15
4	7	3	3	3	3	12	10
5	13	14	13	13	10	50	28

4.2 Backgrounds and systematics

We have not so far discussed the possibility of contaminant signals. For Galactic microlensing surveys, novae and background supernovae pose a potential background contaminant which may be hard to discriminate from microlensing (Alcock et al. 2000). Another potential background comes from Macho events in the Milky Way or M31 dark matter haloes. Here, we argue that these backgrounds are unlikely to be significant for the Angstrom Project.

The POINT-AGAPE M31 dark matter microlensing survey has detected 20 classical novae in 3 yr of data covering an area of 0.6 deg^2, nine of which occurred within 5 arcmin of the bulge centre (Darnley et al. 2004). This represents a potential background of three novae per season, which is already at least an order of magnitude below the predicted stellar microlensing rate. However, none of these novae was mistaken for microlensing by POINT-AGAPE as the light-curves show a high level of asymmetry and strong colour evolution. For a high cadence survey like Angstrom, it is even less likely that such objects would pass reasonable event selection criteria, so we conclude that the potential for false positives from novae is small.

The rate of background supernovae brighter than $V \sim 20$ is known to be about 5 yr^{-1} deg^{-2} [see the discussion in Alcock et al. (2000), and references therein], implying a rate of just 0.15 yr^{-1} within an

11-arcmin field. Again, the majority of supernovae lightcurves ought to be easily distinguishable from microlensing for a high-cadence survey, but the rate is in any case negligible.

Macho microlensing events are potentially a more problematic contaminant. The POINT-AGAPE collaboration has recently published results of a 3-yr search for Machos in M31 (Calchi Novati et al. 2005). They detect two events within 5 arcmin of the centre of M31 and find that their efficiency to Macho lensing events with similar durations to stellar lensing events is around 20 per cent in the bulge region. Since stellar lensing is expected to dominate in the inner bulge region (Kerins et al. 2001; Baltz et al. 2003), even these two events may be stellar events rather than Machos. But even if we assume that they are both Machos, the underlying rate is $\lesssim 3$ events per season, so on this basis Machos should be a relatively small contaminant. Of course, a survey like Angstrom, with its higher cadence, may be sensitive to more Macho events. But, even if the Macho rate turns out to be comparable to that of stellar events (i.e. $\gtrsim 30$ events per season), the resulting combined sample of $\gtrsim 180$ stellar and Macho events over three seasons should allow the two populations to be distinguishable, with stellar events showing a marked spatial concentration.

One systematic factor that can affect the observed event rate is extinction. We have allowed for both foreground and internal extinction in calibrating our M31 models (see Section 3.2). We have also allowed for foreground extinction in computing the M31 distance modulus, but we have ignored internal M31 extinction for our rate calculations. Holwerda et al. (2005) have obtained internal extinction estimates for several nearby spiral galaxies by studying background galaxy counts. They find that extinction estimates are relatively independent of the galaxy inclination angle, which suggests that the dust is confined to a thin sheet in the disc plane. In this case, it is easy to quantify the effect of extinction on microlensing rates. The half of the source population which lies in front of the dust screen is unaffected by the dust. The other half is dimmed by a factor of $10^{-0.4\,A_R} = 0.74$ for an internal extinction of $A_R = 0.33$ mag. From equation (1) we see that, for a fixed galaxy brightness, a 26 per cent reduction in source flux demands a similar reduction in the maximum impact parameter u_t in order for the microlensed source to be detected. Since from equation (4) the microlensing rate scales with u_t then an internal M31 extinction of $A_R = 0.33$ results in an overall reduction of 13 per cent in the observed rate.

5 DISCUSSION

The Angstrom Project is using three telescopes to conduct a high time resolution survey of the bulge of the M31. The principal aim of the survey is to detect microlensing events with durations above 1 d due to low-mass stars and brown dwarfs in the bulge of M31.

We have shown in this study that M31 presents a ripe target for a high time resolution microlensing survey. Using simple analytic models for the disc and bulge of M31, we have shown that a survey like Angstrom should detect around 27 events per season over an 11-arcmin field of view for a standard stellar mass function which is truncated at the hydrogen burning limit. Half of these events have durations below 10 d. If the stellar mass function contains a substantial brown-dwarf population, the expected yield rises to around 64 events per season, with some 80 per cent having durations less than 10 d.

The underlying mass function of the lenses can be probed through the average duration of detected events, as well as through the number of events. Mass functions with dominant brown-dwarf popu-

lations produce shorter events but also necessarily imply a larger mass-to-light ratio and so heavier bulge or disc mass, giving rise to more events.

We find that the events are dominated by bulge lenses and that their spatial distribution provides a good tracer of the bulge geometry. In particular, if the bulge is barred and orientated away from the disc major axis, as suggested by surface brightness measurements, then this should be evident in the spatial distribution of the events. The importance of this is that microlensing directly traces the underlying mass distribution, rather than the light distribution, and so provides a completely independent probe of the underlying bar geometry. Finally, the combination of an offset barred bulge, a highly inclined disc, and different stellar luminosity functions in the disc and bulge is predicted to give rise to a four-way asymmetry in the number of events. Different numbers of events are expected in each of the four quadrants defined by the major and minor axes of the M31 disc.

Aside from probing, the M31 bulge structure and mass function, the high time resolution data from the Angstrom Project should allow for a more efficient detection of exotic microlensing phenomena, such as binary lensing events (Baltz & Gondolo 2001), than is possible with current surveys. It will also be uniquely sensitive to variable stars and transients which undergo outbursts on time-scales of less than 10 d.

REFERENCES

Afonso C. et al., 2003a, A&A, 400, 951
Afonso C. et al., 2003b, A&A, 404, 145
Alard C., Lupton R., 1998, ApJ, 503, 325
Alcock C. et al., 2000, ApJ, 542, 281
An J. et al., 2002, ApJ, 572, 521
Baltz E., Gondolo P., 2001, ApJ, 559, 41
Baltz E., Gyuk G., Crotts A., 2003, ApJ, 582, 30
Binney J., Merrifield M., 1998, Galactic Astronomy. Princeton, New Jersey, p. 192
Bond I. et al., 2004, ApJ, 606, L155
Calchi Novati S. et al., 2003, A&A, 405, 851
Calchi Novati S. et al., 2005, A&A, 443, 911
Darnley M. et al., 2004, MNRAS, 353, 571
Davies R., Frogel J., Terndrup D, 1991, AJ, 102, 1729
de Jong J. et al., 2004, A&A, 417, 461
Dwek E. et al., 1995, ApJ, 445, 716
Fields D. et al., 2003, ApJ, 596, 1305
Girardi L., Salaris M., 2001, MNRAS, 323, 109
Gould A., 1994, ApJ, 435, 573
Gould A., 2000, ApJ, 535, 928
Han C., 1996, ApJ, 472, 108
Holwerda B., Gonzalez R., Allen R., van der Kruit P., 2005, AJ, 129, 1396

E. Kerins et al.

Jablonka P. et al., 1999, ApJ, 518, 627

Joshi Y., Pandey A., Narasimha D., Sagar R., 2005, A&A, 433, 787

Kerins E. et al., 2001, MNRAS, 323, 13

Kent S. M., 1989, AJ, 97, 1614

McElroy D., 1983, ApJ, 270, 485

Paulin-Henriksson S. et al., 2003, A&A, 405, 15

Popowski P. et al., 2005, ApJ, 631, 879

Rich R., Mighell K., 1995, ApJ, 439, 145

Riffeser A., Fliri J., Bender R., Seitz S., Gössl C., 2003, ApJ, 599, 17

Schlegel D., Finkbeiner D., Davis M., 1998, ApJ, 500, 525

Stanek K., Garnavich P., 1998, ApJ, 503, 131

Stark A., Binney J., 1994, ApJ, 426, L31

Stephens A. et al., 2003, AJ, 125, 2473

Sumi T. et al., 2003, ApJ, 591, 204

Sumi T. et al., 2005, ApJ, in press (astro-ph/0502363)

Udalski A. et al., 2003, AcA, 53, 291

Uglesich R. et al., 2004, ApJ, 612, 877

Walterbos R., Kennicutt R., 1987, A&AS, 69, 311

Widrow L., Perrett K., Suyu S., 2003, ApJ, 588, 311

Wyse R., Gilmore G., Franx M., 1997, ARA&A, 35, 637

Zoccali M. et al., 2000, ApJ, 530, 418

This paper has been typeset from a TEX/LATEX file prepared by the author.